Annu. Rev. Phys. Chem. 2002. 53:201–20
DOI: 10.1146/annurev.physchem.53.091801.092924

SCANNING TUNNELING MICROSCOPY STUDIES OF THE ONE-DIMENSIONAL ELECTRONIC PROPERTIES OF SINGLE-WALLED CARBON NANOTUBES

Min Ouyang,[1] Jin-Lin Huang,[1] and Charles M. Lieber[1,2]
[1]Department of Chemistry and Chemical Biology and [2]Division of Engineering and Applied Science, Harvard University, Cambridge, Massachusetts 02138; e-mail: cml@cmliris.harvard.edu

Key Words SWNTs, STM, band structure, energy gaps, resonant scattering, Kondo

■ **Abstract** Recent developments in scanning tunneling microscopy studies of the electronic properties of single-walled carbon nanotubes are reviewed. A broad range of topics focused on the unique electronic properties of nanotubes are discussed, including (*a*) the underlying theoretical description of the electronic properties of nanotubes; (*b*) the roles of finite curvature and broken symmetries in perturbing electronic properties; (*c*) the unique one-dimensional energy dispersion in nanotubes; (*d*) the nature of end states; (*e*) quantum size effects in short tubes; (*f*) the interactions between local spins and carriers in metallic systems (the Kondo effect); and (*g*) the atomic structure and electronic properties of intramolecular junctions. The implications of these studies for understanding fundamental one-dimensional physics and future nanotube device applications are discussed.

INTRODUCTION

Single-walled carbon nanotubes (SWNTs) have aroused great excitement as unique systems for understanding one-dimensional (1D) physics and for building carbon-based nanoelectronics (1–4). The inherent high aspect ratio of SWNTs makes these materials ideal scanning probe microscope tips (5, 6), and mechanical measurements have demonstrated that carbon nanotubes have the largest Young's modulus of any known material (7, 8). However, it is the electronic properties of SWNTs, which depend uniquely on geometric structure, that are arguably the most significant characteristic of this material. A single SWNT can be either metallic or semiconducting (9–15), depending only on diameter and chirality, although the local carbon-carbon bonding remains constant. The ability to yield both metallic and semiconducting forms without doping is unique among solid-state materials, and has led to speculation that SWNTs might thus serve as a building block for carbon-based electronics (4).

A large number of measurements have been carried out in attempts to verify the remarkable electronic properties predicted for SWNTs (13, 14, 16–18), although the first clear elucidation of metallic and semiconducting SWNTs was obtained from scanning tunneling microscopy (STM) studies (13, 14). STM has proven to be exceptionally well suited for the elucidation of the fundamental electronic properties of SWNTs because it can determine simultaneously both the atomic structure and local electronic density of states (DOS). Initial STM studies of SWNTs focused on the interrogation of the basic relationship between atomic structure and electronic properties (3, 13, 14), and subsequently investigated the structures of SWNT ends and the consequences of finite size (3, 19, 20). Most recently, STM investigations have begun to address more fundamental issues about the electronic properties of SWNTs (15, 21–23), including the determination of unique 1D energy dispersion predicted for this material.

Herein, we review the fascinating electronic properties of SWNTs and discuss the implications of these properties for future electronics. The review is organized as follows: First, a π-only tight-binding scheme is presented to explain the basic electronic properties of SWNTs and to provide a framework for interpreting STM studies; second, experimental and theoretical studies addressing the roles of finite curvature and broken symmetries in perturbing the electronic properties of SWNTs are discussed; third, studies of energy-dependent resonant scattering, which enable the unique 1D energy dispersion to be characterized, are presented; fourth, the structure and electronic states of SWNT ends and quantum effects in finite size SWNTs are discussed; fifth, the interactions between local spins and carriers in metallic and finite size SWNTs are described; and sixth, the atomic structure and electronic properties of intramolecular semiconductor-metal and metal-metal junctions are presented. In concluding, implications of these studies for understanding fundamental 1D physics and future nanotube device applications are discussed.

THEORETICAL BACKGROUND

A SWNT can be viewed as a seamless cylinder obtained by rolling-up a single layer of a two-dimensional (2D) graphene sheet. The SWNT is uniquely characterized by the roll-up vector, $\mathbf{C_h} = n\mathbf{a_1} + m\mathbf{a_2} \equiv (n, m)$, where $\mathbf{a_1}$ and $\mathbf{a_2}$ are the graphene primitive vectors and n, m are integers (Figure 1). The translation vector, $\mathbf{T}$, is directed along the SWNT axis and perpendicular to $\mathbf{C_h}$; the magnitude of $\mathbf{T}$ corresponds to the length of the (n, m) SWNT unit cell. Once (n, m) is specified, other structural properties, such as diameter (d_t) and chiral angle (θ), can be determined: $d_t = (3^{1/2}/\pi)a_{cc}(m^2 + mn + n^2)^{1/2}$; and $\theta = \tan^{-1}[3^{1/2}m/(2n + m)]$, where a_{cc} is the nearest-neighbor carbon atom distance of 0.142 nm. Among the large number of possible $\mathbf{C_h}$ vectors, there are two inequivalent high symmetry directions. The two high symmetry tubes are called zigzag and armchair (Figure 1), and are designated by (n, 0) and (n, n), respectively. These tubes are achiral; however, when $\mathbf{C_h}$ lies along a lower symmetry direction, the corresponding SWNTs will be chiral.

The electronic band structure of SWNTs can be analyzed using a tight-binding model, in which hybridization effects due to the finite curvature of the tube structure are ignored. With this approximation the tight-binding Hamiltonian H(***k***) is (24):

$$\mathrm{H}(\boldsymbol{k}) = \sum \gamma_0 \mathrm{e}^{\mathrm{i}\boldsymbol{k}\bullet\mathbf{r}_\mathrm{i}}, \qquad 1.$$

where γ_0 is the amplitude of the nearest-neighbor overlap integral, and $\mathbf{r}_\mathrm{i}$ (i = 1, 2, 3) are the bond vectors of the graphene sheet. The π and π^* band energy dispersions obtained using this model are:

$$\mathrm{E}_{\mathrm{cv}}(k_\mathrm{x}, k_\mathrm{y}) = \pm\gamma_0\left\{1 + 4\cos\left(3k_\mathrm{x}a_{\mathrm{cc}}/2\right)\cos\left(3^{1/2}k_\mathrm{y}a_{\mathrm{cc}}/2\right)\right.$$
$$\left. + 4\cos^2\left(3^{1/2}k_\mathrm{y}a_{\mathrm{cc}}/2\right)\right\}^{1/2}, \qquad 2.$$

where $+(-)$ corresponds to the π^* (π) bands. Figure 2*a* shows the 2D graphene sheet band structure in the first Brillouin zone obtained from Equation 2. The Fermi surface of graphene sheet determined from $\mathrm{H}(\boldsymbol{k}_\mathbf{F}) = 0$ is reduced to the six corners ($\mathbf{K_B}$) of the hexagonal first Brillouin zone (Figure 2*b*). Because there are two atoms per unit cell, the valence band of graphene is completely filled.

The 1D band structure of a SWNT can be derived from this 2D model by imposing periodic boundary conditions. All allowed wavevectors ***k*** are quantized in the direction perpendicular to the rolled-up vector $\mathbf{C_h}$: $\boldsymbol{k}\bullet\mathbf{C_h} = 2\pi\mathrm{q}$, where q is an integer. Therefore, only a particular set of lines, which are parallel to the corresponding tube axis with a spacing of $2/\mathrm{d_t}$, are allowed (Figures 2*c*, 2*d*). If the allowed wavevector passes through Fermi points $\mathbf{K_B}$ of the graphene sheet, the SWNT is predicted to be metallic, and otherwise semiconducting. From the criteria $\mathbf{K_B}\bullet\mathbf{C_h} = 2\pi\mathrm{q}$, we thus expect:

$$\begin{cases} \mathrm{n} - \mathrm{m} = 3\mathrm{q}\text{: metallic} \\ \mathrm{n} - \mathrm{m} \neq 3\mathrm{q}\text{: semiconducting.} \end{cases} \qquad 3.$$

The 1D band structure of SWNTs can be constructed by zone-folding the 2D graphene band structure into the 1D Brillouin zone of a (n, m) SWNT (1, 19). The allowed states for the (n, m) SWNT lie on a set of parallel lines in the reciprocal space along the tube axis. The first Brillouin zone of a (n, m) SWNT is determined from the translation vector $\mathbf{T}$ with the length of $2\pi/|\mathbf{T}|$; that is, the segment between $\pm\pi/\mathbf{T}$ (Figure 3). The π and π^* bands of the SWNT are obtained by assuming the values of Equation 2 along this line segment. The remaining bands are generated by zone folding using:

$$\mathrm{E}_\mu(k) = \mathrm{E}_{\mathrm{cv}}\left(k\mathbf{T}/|\mathbf{T}| + \mu(2\pi)\mathbf{C_h}/|\mathbf{C_h}|^2\right)$$
$$(\mu = 0, \ldots, \mathrm{N}-1, \quad \text{and} \quad -\pi/|\mathbf{T}| < k < \pi/|\mathbf{T}|), \qquad 4.$$

where N is the number of hexagons in the nanotube unit cell, which is determined by $\mathrm{N} = |\mathbf{C_h} \times \mathbf{T}|/|\mathbf{a_1} \times \mathbf{a_2}|$.

The DOS of SWNTs can be computed from the band structure by summing the number of states at every energy level (Figure 3). The calculated DOS of SWNTs exhibit a distinct signature of 1D systems; that is, divergent singularities that are commonly referred to as van Hove singularities (VHS) (25). In three dimensions (3D), VHS should appear as kinks, although in 2D they appear as stepwise discontinuities. Hence, the VHS in 1D SWNTs represent well-defined (spike-like) features that should enable direct clear comparisons between experiment and theory.

Lastly, there are several other important characteristics of the electronic properties of SWNTs suggested by π-only tight-binding models (3, 26–28). First, the DOS at E_F has a zero value for semiconducting SWNTs ($n - m \neq 3q$) but is nonzero (and small) for metallic SWNTs ($n - m = 3q$). Second, the VHS spacing has a characteristic 1–2–4 pattern from E_F (with spacing 1ξ–2ξ–4ξ) for semiconducting SWNTs, and 1–2–3 from E_F (with spacing 3ξ–6ξ–9ξ) for metallic SWNTs, where $\xi = 2\pi/3|\mathbf{C_h}|$. Third, the first VHS band gaps for semiconducting and metallic SWNTs are $E_g^S = 2\gamma_0 a_{cc}/d_t$ and $E_g^M = 6\gamma_0 a_{cc}/d_t$, respectively, and are independent of chiral angle θ to first order.

INITIAL SCANNING TUNNELING MICROSCOPY STUDIES

The first studies that directly addressed these theoretical predictions were carried out by Odom et al. (13) and Wildöer et al. (14) using low-temperature STM. These initial STM studies characterized both the atomic structures and the DOS of individual SWNTs and SWNTs packed in bundles, and showed the existence of both semiconducting and metallic SWNTs for a wide range of structures as predicted by theory. Subsequently, Kim et al. (19) and Odom et al. (3) reported the first detailed comparisons of experimentally determined SWNT VHS with tight-binding calculations for metallic and semiconducting tubes. The good agreement between theory and these experiments showed that much of the physics of SWNT band structure is captured by the simple π-only model. However, other important issues, such as the effects of finite curvature and broken rotational symmetry, which are essential to a complete understanding of the electronic properties and potential device applications of SWNTs, were not addressed. We examine these and other fascinating questions below.

FINITE CURVATURE EFFECT OF SINGLE-WALLED CARBON NANOTUBES

Theoretical Models

As the diameter of a SWNT decreases, the hybridization between orthogonal molecular orbitals cannot be neglected. For a SWNT with sufficiently small diameter, the hybridization of σ, σ^*, π and π^* orbitals can be quite large (29). Full-valence tight-binding calculations (30) and analytical calculations for a

Hamiltonian on a curved surface have suggested that the finite curvature of SWNTs (31) will strongly modify the electronic behavior of SWNTs and open up small energy gaps at E_F.

To understand the effect of finite curvature more directly, Ouyang et al. (15) and Kleiner & Eggert (32) have independently developed a Fermi-point shifting model in which finite curvature or tube deformation (33) produces shifts of the Fermi points from $\mathbf{K_B}$ (Figure 4). In general, when the bond symmetry of neighboring carbon atoms is broken, the corresponding nearest-neighbor overlap integral, γ_0, is no longer constant and can be expressed as $\gamma_i = \gamma_0 + \Delta\gamma_i$ ($i = 1, 2, 3$). Here, the $\Delta\gamma_i$ are estimated from misalignment angle α, which describes the misorientation of neighboring atoms (Figure 4*a*) and is determined by the local curvature. The corresponding Hamiltonian can be written as

$$H'(\boldsymbol{k}) = \sum \gamma_i e^{i\boldsymbol{k}\bullet\mathbf{r}_i}, \qquad 5.$$

where the Fermi points with curvature are given by $H'(\boldsymbol{k_F}) = 0$. For small changes of γ_i, we expect that the shift of $\boldsymbol{k_F}$ is small and can be given as $\boldsymbol{k_F} = \mathbf{K_B} + \Delta\boldsymbol{k_F}$. The magnitude and direction of $\Delta\boldsymbol{k_F}$ enable the role of curvature to be quantified. For a metallic zigzag (n, 0) SWNT, the magnitude is:

$$\begin{aligned} |\Delta\boldsymbol{k_F}| = &\left\{3^{1/2}\pi^2 \Big/ \left[a_{cc}(12n^2 + \pi^2)\right]\right\} \\ &-\left\{\pi^3(8n^2 + \pi^2)^{1/2} \Big/ \left[3^{1/2}a_{cc}n^2(48n^2 + 4\pi^2)\right]\right\} \end{aligned} \qquad 6.$$

and the direction of $\Delta\boldsymbol{k_F}$ is perpendicular to the tube axis along the circumferential direction **c** (Figure 4*b*). From this shift the energy gap width can be defined as

$$E_g^c = \left[3\gamma_0 a_{cc}^2 \Big/ (16R^2)\right], \qquad 7.$$

where R is the radius of the SWNT.

In addition, the energy dispersion near E_F under finite curvature effect remains linear,

$$|E(\boldsymbol{k})| \propto \left(3^{1/2}\gamma_0 a_{cc}\right)[1 + \pi^2/(8n^2)]|\boldsymbol{k} - \boldsymbol{k}_F|, \qquad 8.$$

and thus the DOS near E_F can be expressed as a universal function (28, 34):

$$\begin{cases} \rho(E) \propto |E| \Big/ \left[|E|^2 - E_g^{c2}/4\right]^{1/2} & \text{for } |E| > E_g^c \\ 0 \quad \text{for } |E| < E_g^c. \end{cases} \qquad 9.$$

In summary, our Fermi-point shifting model predicts that metallic zigzag tubes are in fact small gap semiconductors.

We have also applied this model to armchair (n, n) SWNTs with finite curvature (Figure 4*c*). In contrast to zigzag SWNTs, the symmetry of armchair

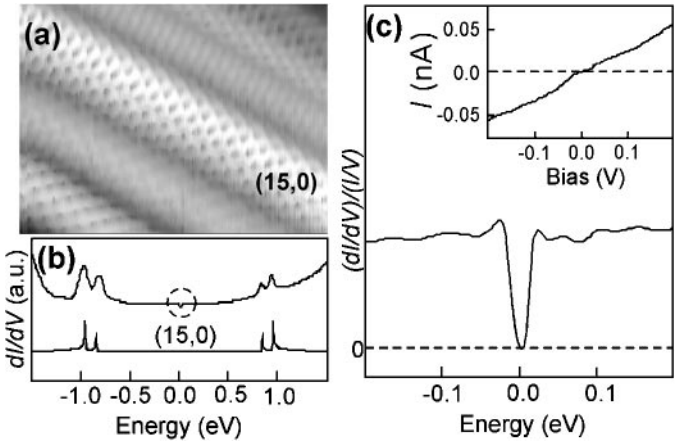

Figure 5 (*a*) Atomically resolved constant current STM image of a (15, 0) SWNT. (*b*) Tunneling conductance, dI/dV, for (15, 0) zigzag SWNTs, with corresponding calculated DOS shown below. The new feature near E_F is highlighted with a dashed circle. (*c*) High energy resolution normalized conductance, $(dI/dV)/(I/V)$, and measured *I–V* curves (inset) for the (15, 0) tube.

SWNTs requires that $\Delta \boldsymbol{k_F}$ is perpendicular to **c** and along the tube axis. Hence, even with finite curvature, the new Fermi points of an armchair SWNT still lie on the allowed wavevectors and suggest that an isolated armchair SWNT will remain truly metallic.

Experimental Studies of Curvature-Induced Gaps

Ouyang et al. carried out the first direct studies of curvature-induced gaps in SWNTs using low-temperature STM (15). Figure 5*a* shows a typical atomically resolved image of a (15, 0) SWNT. The VHS determined experimentally and calculated using a π-only tight-binding model show excellent agreement (Figure 5*b*), and suggest that finite curvature does not perturb the larger energy features of the SWNT electronic structure. However, these data also show a reduction in the DOS or gap-like feature near E_F. High-resolution normalized tunneling spectra, which are proportional to the local DOS, clearly show that the local DOS at E_F are reduced to zero (i.e., a true energy gap) with sharp increases at energies that depend inversely on the zigzag tube radius. Values of the energy gaps for different zigzag SWNT radii were determined using Equation 9 broadened with a Gaussian convolution to account for instrumentation and temperature effects (Figure 6) (15), and are well fit by the $1/R^2$ dependence predicted by Equation 7.

Lastly, these studies have enabled γ_0 to be determined independently by studying the radius dependence of gap widths. The value obtained from a fit to Equation 7, 2.60 eV, is in good agreement with the range of 2.5–2.7 eV determined in

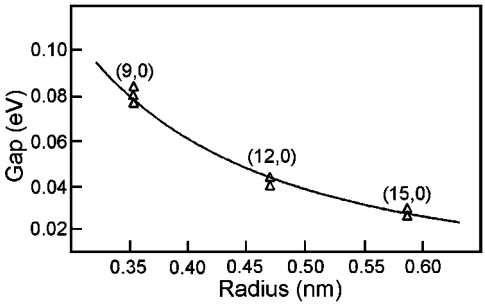

Figure 6 Curvature-induced energy gaps vs. tube radius. Every data point (triangle) represents the averaged gap value for one distinct (n, 0) SWNT. The solid line corresponds to a fit of $3\gamma_0 a_{cc}{}^2/(16R^2)$ with γ_0 value of 2.60 eV. Adapted from Reference 15.

earlier STM studies (13, 14). In summary, these experimental studies have shown conclusively that predicted metallic (n, 0) SWNTs are actually narrow gap semiconductors.

BROKEN SYMMETRY: ARMCHAIR SWNTs

The Fermi-point shifting model suggests that finite curvature will not affect the metallic nature of isolated armchair SWNTs. This suggestion is consistent with atomically resolved, low-temperature STM investigations (15) of isolated (8, 8) SWNTs (Figure 7*a*). These studies showed the local DOS was nonzero and constant at E_F, and thus the SWNT was metallic (Figure 7*b*). In contrast, studies of armchair SWNT bundles by Odom et al. (3) and Ouyang et al. (15) first reported the existence of a small energy gap feature near the E_F. For example, the local DOS measured for a (8, 8) SWNT packed in the bundle (Figures 7*b*, 7*d*) show a clear suppression around E_F in contrast to the data for the isolated (8, 8) SWNT. Comparison of these data with the calculated and experimental DOS of an isolated (8, 8) SWNT shows good agreement for the position of the VHS peaks, which suggests that the isolated and bundle tubes have very similar electronic band structure for greater energies, >0.1 eV. This comparison thus suggests that tube-tube interactions do not perturb the electronic band structure on larger energy scales.

High-resolution data recorded near E_F on the (8, 8) SWNT in the bundle show that the gap has a magnitude of $\sim$100 meV (Figure 7*d*). The gap structure observed in armchair tubes in bundles differs from the finite curvature-induced gaps in zigzag SWNTs discussed above. Specifically, the local DOS are suppressed but not reduced completely to zero, and for this reason, these gaps are termed pseudogaps (15). Similar gap features were observed in other armchair SWNT bundles (Figure 8*a*), with gap values ranging from 80 to 100 meV in the (10,10) through (7, 7) SWNTs, respectively (Figure 8*b*).

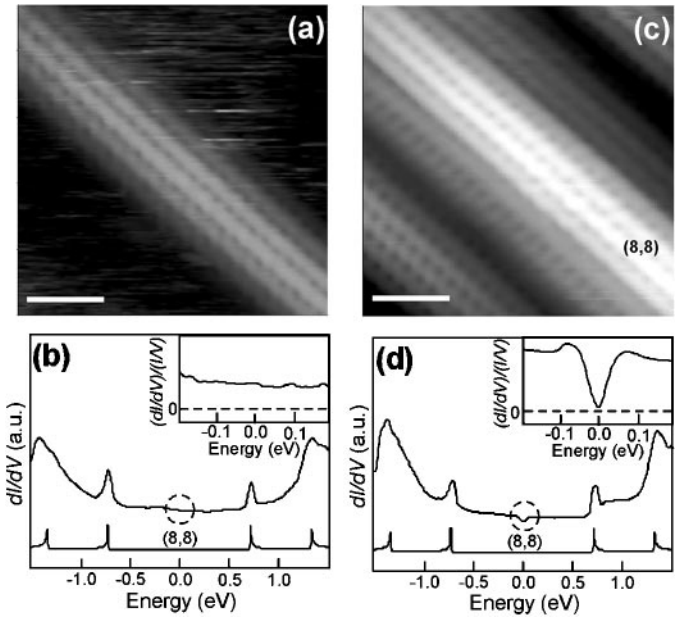

Figure 7 (*a*) STM image of an isolated (8, 8) SWNT on Au(111) substrate. Scale bar is 1 nm. (*b*) (dI/dV) recorded on the isolated (8, 8) tube. The calculated DOS for an isolated (8, 8) tube is displayed below the experimental data. The dashed circles highlight the energy near E_F. (*Inset*) High-resolution $(dI/dV)/(I/V)$ data near E_F. (*c*) STM image of an (8, 8) SWNT exposed at the top of a bundle. Scale bar is 1 nm. (*d*) Same as (*b*) but data recorded on (8, 8) tube in the bundle of (*c*).

The appearance of pseudogaps in the armchair SWNTs is at first glance surprising, but can be understood in terms of the broken n-fold rotational symmetry of armchair SWNTs due to interactions in a bundle (15) (Figure 8*c*). Briefly, in an isolated armchair SWNT, π and π^* bands have different parity under reflection and cross at the E_F without opening a gap (27). However, when the armchair tubes are packed into a bundle, strong tube-tube interactions (26, 35–38) will break rotational symmetry and enable mixing of π and π^* bands and the formation of a pseudogap at E_F. Theoretical studies of armchair SWNT bundles (26, 35–38) have predicted the existence of pseudogaps at E_F, and our measured pseudogaps have similar magnitudes (Figure 8*b*). In addition, our experimental data exhibit a weak inverse dependence on SWNT radius, which is qualitatively consistent with theoretical predictions (37). However, deviations between experiment and theory are also clear when making detailed comparisons. One possible origin for these differences is that STM experiments were carried out on SWNTs at the surfaces of bundles, whereas theoretical calculations have been based on periodic lattices with higher local coordination. Future calculations

carried out on structures accurately modeling STM experiments should help to address such differences.

Lastly, our experimental studies enable several important points to be addressed. First, experimental evidence for true 1D metallic behavior in isolated armchair tubes on Au(111) substrates implies that the tube-substrate interaction does not perturb strongly the band structures of nanotubes (3). Second, the presence of sizeable pseudogaps in armchair tube bundles will modify electrical transport, and the very low DOS at E_F will make extended states in such tubes susceptible to localization. From a positive perspective, the existence of pseudogaps in armchair SWNTs should make these samples sensitive to doping, which may enable their use in sensor applications.

1D ENERGY DISPERSION

SWNTs are predicted to exhibit a unique linear energy dispersion at low energies ($E/\gamma_0 \ll 1$), which contrasts with the parabolic dependence expected from a conventional free-electron picture, and will impact significantly electronic behavior near E_F. In the case of isolated armchair (n, n) SWNTs, their metallic nature arises from the linear crossing of π and π^* energy bands at E_F. However, experimental determination of this important characteristic of the band structure has been lacking. Use of conventional momentum analysis methods, which average over substantial area, is difficult because SWNT samples consist of a wide range of structures each with different energy dispersions (3, 13–15, 39). STM, which can be used to interrogate individual nanotubes and has been used previously to determine the energy dispersions of 2D surface states on metals (40, 41) and semiconductors (42, 43), can, however, address this critical point.

Modulations in the local DOS of 1D metallic SWNTs near defects (3, 23, 44) and at the tube ends (45) have been observed in STM studies, and qualitatively attributed to the interference between incident and scattered electron waves in the nanotubes. However, these studies did not investigate the energy dependence of the DOS modulations, which would be needed to probe the 1D energy dispersion. Ouyang et al. first applied the STM to elucidate the 1D energy dispersion of SWNTs by characterizing in detail energy-dependent quantum interference of electrons scattered by defects in metallic nanotubes (22).

High-resolution STM images (Figure 9*a*) of an armchair SWNT with a defect show clearly a strong modulation in the DOS around the defect with a period larger than that of the armchair atomic lattice. Tunneling spectra (Figure 9*b*) recorded away from the defect ($\sim$8 nm) exhibit the VHS features characteristic of an isolated (13, 13) SWNT. Significantly, tunneling spectra recorded near the defect region show nine additional low-energy peaks (Figure 10). The most striking aspect of these peaks in the DOS is that their amplitude varies along the SWNT axis; these oscillations can be seen clearly in plots of the DOS vs. position for fixed energies

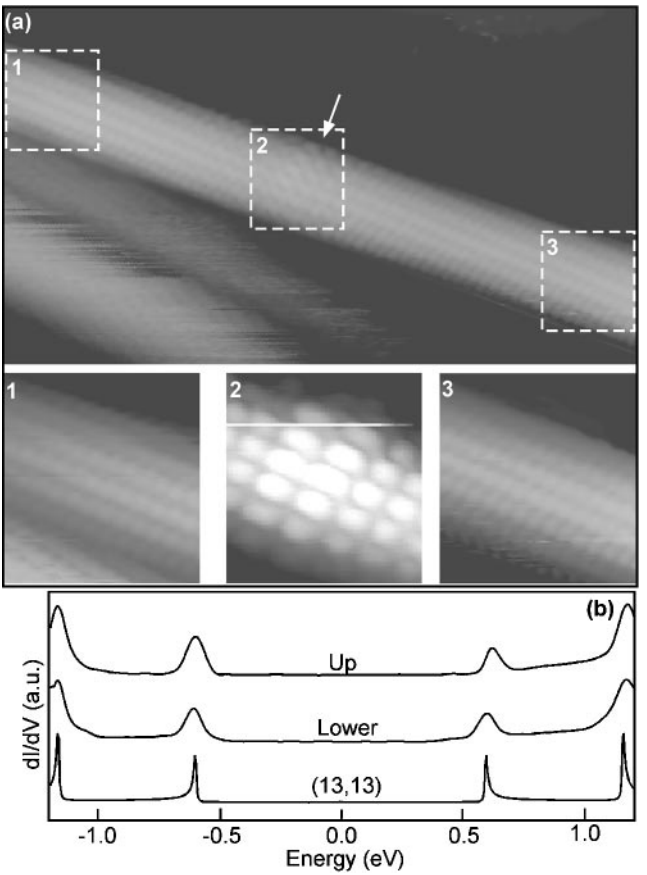

Figure 9 (*a*) (*Upper*) Atomically resolved STM image of an isolated armchair SWNT containing one defect; three numbered dashed squares highlight different regions along the tube axis. The white arrow highlights the defect position. (*Lower*) High-resolution images corresponding to the three distinct areas in upper panel. (*b*) dI/dV data recorded on the upper and lower portions of the tube ~8 nm away from the central defect area, and the calculated DOS for an isolated (13, 13) armchair SWNT.

(Figure 11). Qualitatively, these data also show that the oscillation wavelength decreases as the energy increases.

The observation of DOS oscillations at specific energy values is consistent with resonant electron scattering. Resonant scattering from defect-related quasibound states has been reported in recent SWNT theoretical studies (46) and transport measurements (47). We have developed this idea to understand quantitatively the DOS oscillations observed in STM studies (22). First, a specific energy-dependent oscillation is modeled using a 1D plane wave e^{ikx} (where x is position) with an energy equal to that of a defect quasibound state and incident on the defect at

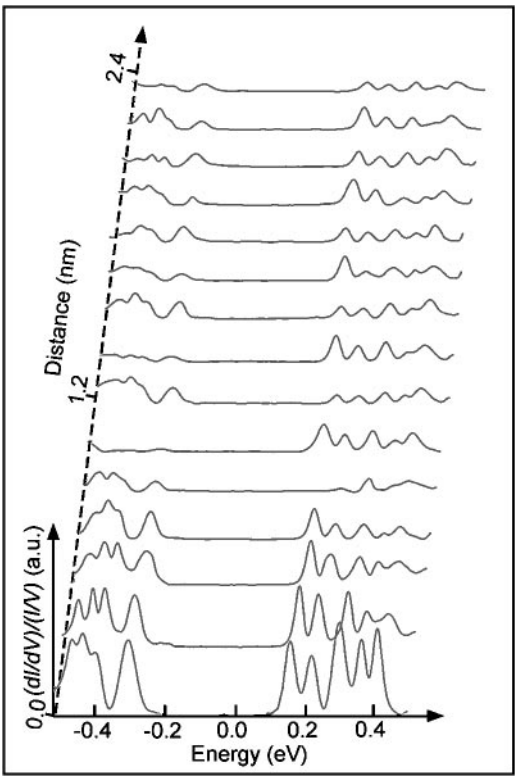

Figure 10 $(dI/dV)/(I/V)$ vs. energy recorded as a function of distance from the defect in Figure 9. Curves start at the central defect position (white arrow position in Figure 9) and progress along the upper left portion of the nanotube.

$x = 0$. Second, the incident plane wave can resonantly backscatter from the quasibound state with a reflectivity $|R|^2$ ($R = |R|e^{-i\delta}$, where δ is the phase shift). The corresponding standing wavefunction is written as $\psi(k, x) = e^{ikx} + |R|e^{-i(kx+\delta)}$, which corresponds to a spatial oscillation in the DOS, $\rho(k, x)$:

$$\rho(k, x) = |\psi(k, x)|^2 = 1 + |R|^2 + 2|R| \cos(2kx + \delta). \qquad 10.$$

In addition, processes such as electron-electron (e-e) and electron-phonon (e-ph) interactions can dephase the wave and lead to a decay of the interference (48). Including a phenomenological dephasing coherence length l_φ, we rewrite $\rho(k, x)$ as:

$$\rho(k, x) = |\psi(k, x)|^2 = 1 + |R|^2 + 2|R| \cos(2kx + \delta)e^{-2x/l\varphi}. \qquad 11.$$

We have found this model provides excellent fits to all energy-dependent oscillations (Figure 11) (22). Significantly, these fits provide values for $E(k)$ vs. k, and demonstrate that this dispersion is indeed linear near E_F (Figure 12). The experimental energy dispersion agrees well with the linear dispersion

predicted for armchair SWNTs (27), $|E(k)| = (3/2)a_{cc}\gamma_0|k - k_F|$. Such fitting also yields values of $\gamma_0 = 2.51$ eV and $k_F = 8.48 \pm 0.05$ nm^{-1}. This γ_0 value is in good agreement with previous experimental values from STM studies (13–15), and the value of k_F is consistent with the predicted value $k_F = 2\pi/(3^{3/2}a_{cc}) = 8.52$ nm^{-1} for an armchair SWNT (1). In addition, deviations in the fits close to the defect exist, although these are likely due to the simplified model used to treat defects; more detailed theoretical treatments that explicitly account for defect structure could provide further insight into this issue in the future.

Lemay et al. recently also reported an STM study of 1D energy dispersions of metallic SWNTs by imaging the wavefunctions in finite size (~40 nm) nanotubes (49). The physical principle behind this study is actually the same as our quantum interference method: the ~40-nm-long tubes can be taken as the system with two defects (both ends), which act as the total or partial reflection boundary for those two pairs of Bloch waves, and therefore the defect scattering picture still holds. However, this study focused on chiral tubes packed in a bundle and neglected the significant effects of finite curvature and tube-tube interactions reviewed above. These important issues will need to be evaluated to draw more meaningful conclusions in the future.

In the case of the data of Ouyang et al. (22), comparison of the experimental energy dispersion with the band structure calculated for a (13, 13) SWNT reveals an excellent agreement between reported experimental data and theoretical π^* band, but no data overlap with the π band. The absence of the π band can be understood in terms of parity matching (50), and further reveals an interesting but important relationship between the defect parity and the symmetry of the energy bands in armchair SWNTs. Specifically, the π and π^* bands of armchair SWNTs have opposite parity because they are constructed from rotationally invariant combinations of symmetric and antisymmetric sums of p_z orbitals. Therefore, if the defect in Figure 9 has odd parity, electrons in the π band (even parity) will not be scattered by the defect, whereas electrons in the π^* band (odd parity) can be scattered when their energies match a defect quasi-bound state. This interesting parity effect was supported by several observations: (*a*) The defect does not break the structural symmetry of the SWNT [i.e., both sides of the defect are consistent with (13, 13) armchair nanotubes], which prevents mixing of π and π^* bands; (*b*) analysis of the position- and energy-dependent local DOS data obtained from the other side of the SWNT yields the same π^* energy dispersion as plotted in Figure 12. Hence, we believe resonant scattering represents an exciting approach for investigating fundamental issues of parity and symmetry breaking in 1D SWNTs.

SWNT END STATES

Similar to the surface of a 3D structure and the edge of a 2D system, the ends of SWNTs can be treated as the surface of the 1D system, which reduces the symmetry of the tube and produces corresponding end states. Therefore, to understand

thoroughly the electronic properties of SWNTs, knowledge of end states is necessary. In general, there are two different types of end states (51): localized and delocalized (i.e., resonant) states. If the energy of an end state falls within the energy gap of semiconducting SWNTs, it will be localized with the wavefunction decaying exponentially into the tube. Alternatively, if the energy of the end state is coincident with a bulk band, this state can connect to the extended bulk state and is delocalized.

Kim et al. (19) reported the first detailed investigations of atomic structure and electronic properties of SWNT ends. In these studies, tunneling spectra data recorded on a metallic (13, −2) SWNT showed two new peaks at 250 and 500 meV near the SWNT end. To investigate the origin of the SWNT end state and identify the specific end structure, Kim et al. further developed different cap models of SWNTs based on the Euler's rule and isolated pentagon rule (52), and carried out the numerical π-only tight-binding calculations for all possible models to compare with experimental data. Significantly, these studies demonstrated clearly that a specific topological arrangement of pentagons could be attributed to low energy peaks in the DOS at the SWNT end.

The decay of the end states was also quantified in this study (19), by examining the tip-nanotube separation, h(x), as a function of position, x, which is proportional to the DOS

$$\exp[k_{\mathrm{d}}\mathrm{h(x)}] \propto \int_0^{eV} \rho(\mathrm{x},\ \mathrm{E})\mathrm{dE}, \qquad 12.$$

where k_{d} is the characteristic inverse decay length. Comparison of experimental $\exp[k_{\mathrm{d}}\mathrm{h(x)}]$ at the peak energies of 250 and 500 meV with integration of the calculated DOS showed good agreement with experimental data, with a characteristic decay length scale ∼10.2 nm (19). These functions also retain a finite magnitude in the bulk, which suggests that they correspond to resonant states.

In addition, there are many open and interesting questions about the properties of SWNT ends. For example, how do the electronic characteristics of end states differ for capped vs. open ends, and how do these differences affect the coupling to metals and/or the emission of electrons? Field emission properties of nanotubes, which have been recently demonstrated (53, 54), could be strongly influenced by the presence of localized or resonant end states (55), and hence such fundamental knowledge could impact significantly this application area.

FINITE SIZE EFFECTS

As the length (L) of a SWNT is reduced, one ultimately will reach the limit of a molecular cluster. Changes in the electronic properties as this finite size regime is approached are of importance to our fundamental understanding and to potential applications. At first order, the effect of finite size or length can be analyzed with a 1D "particle-in-a-box" model, where a tube of length L has a set of discrete wavevectors given by $\boldsymbol{k} = \mathrm{n}\pi/\mathrm{L}$ (n is integer), and corresponding energy level

spacing of $\Delta E = \hbar \Delta k = h v_F / 2L = 1.67$ eV/L (nm), where $v_F = 8.1 \times 10^5$ m/s is the Fermi velocity of graphene (1).

Finite size SWNTs can be prepared by using a voltage pulse between an STM tip and SWNTs to cut a long nanotube into short pieces (3). With this technique, Venema et al. (20, 56) reported discrete energy levels due to the quantum confinement in a L ~30 nm armchair SWNT. Odom et al. carried out more detailed and comprehensive studies of both semiconducting and metallic SWNTs, with lengths down to and below 10 nm (3). Studies of different length metallic SWNTs showed well-defined steps in I/V curves, which were attributed to the resonant tunneling through discrete eigenstates of the finite size SWNTs (Figure 13). The energy level spacing for 6 and 5 nm tubes, 300 and 370 meV, respectively, agreed quantitatively with the particle-in-a-box model. However, data recorded on an ultra-short 3 nm SWNT showed distinct deviation from this simple model. Both ab initio (57) and semi-empirical calculations (58, 59) have predicted that SWNTs <4 nm may deviate owing to asymmetry and shifting of the linear bands crossing at E_F, which could open a gap around E_F. Therefore, the unusual energy level structure observed for the 3 nm SWNT (3) could signify the transition to a system truly molecular in nature and represents an important area to address in the future.

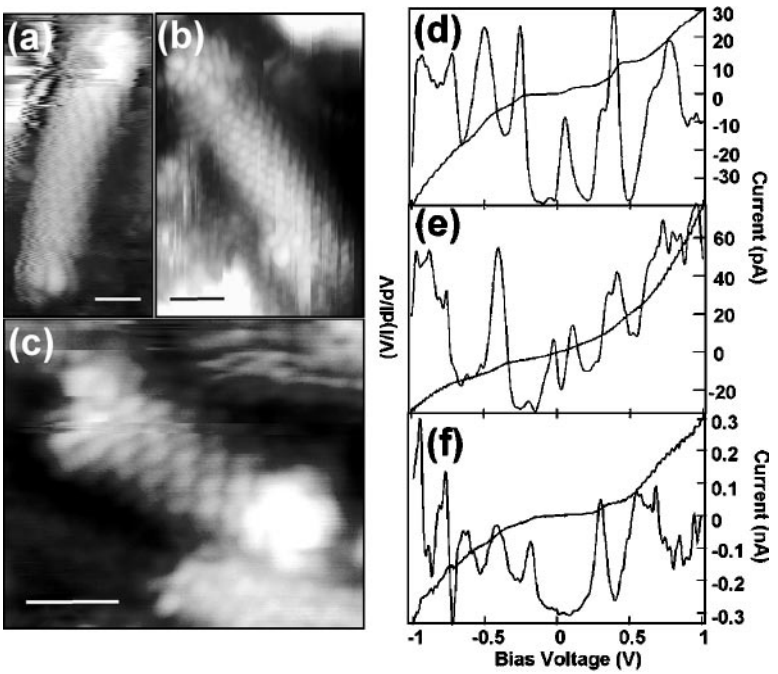

Figure 13 (*a–c*) STM images of SWNTs cut to lengths of 6 nm, 5 nm, and 3 nm, respectively. (*d–f*) I–V and normalized conductance data recorded on the SWNTs in (*a–c*), respectively. Adapted from Reference 3.

On the other hand, semiconducting SWNTs (T.W. Odom, J.L. Huang, & C.M. Lieber, unpublished manuscript) have not shown significant finite size effect as observed in metallic SWNTs (60). Even for a 3 nm ultra-short semiconducting SWNTs, the tunneling spectra measured in the middle of the tube shows almost the same VHS features as the bulk system. Qualitatively, the observation of semiconducting SWNTs in our studies is consistent with theoretical predictions (62) that semiconducting SWNTs have electron mean free paths of only several nanometers, and thus the distinction between bulk and finite size may be more difficult to make (63). Nevertheless, we believe this represents an important issue, which lies at the intersection of molecular and extended systems, to address in the future.

KONDO PHENOMENA IN 1D

A fundamental issue that can now be addressed owing to the availability SWNTs is how 1D electron systems respond to a local spin; that is, the Kondo effect in 1D. The Kondo effect, which describes the interaction between a magnetic moment and conduction electron spins of a nonmagnetic host, is a well-known phenomenon that leads to anomalous transport behavior in bulk systems of dilute magnetic alloys (64). Below the Kondo temperature, T_K, electrons of the host tend to screen the local spin of the magnetic impurity, resulting in the emergence of a Kondo resonance. The Kondo resonance for 2D systems was recently observed in STM investigations of magnetic atoms on noble metal surfaces (65–67).

Odom et al. first took advantage of the metallic SWNTs as 1D metallic hosts to study the interaction between the local spin on Co clusters and extended as well as finite size SWNTs (21). STM images showed that Co clusters could be readily observed on atomically resolved metallic SWNTs (Figure 14*a*), and spectroscopy data recorded directly above a cluster exhibited a strong resonance peak near E_F. Spatially resolved measurements further showed that these peak features systematically decrease in amplitude and ultimately disappear after several nanometers (Figure 14*b*). The new resonance peaks were not observed with nonmagnetic Ag clusters or with Co clusters on semiconducting SWNTs (21), which demonstrates that the observed peaks are due to the interaction of magnetic spins with the SWNT conduction electrons. In addition, analyses of the resonances revealed new information about the effect of dimensionality compared with 2D systems (65–67). In the 2D systems, the Kondo resonance is usually evident as a dip or antiresonance in the tunneling conductance, although in the measurement of Co on SWNTs the Kondo resonance always appears as a sharp peak. This difference can be qualitatively understood in terms of the small number of continuum final states available for tunneling in a SWNT vs. a noble metal (21, 65–67).

Finite size SWNTs have also provided an opportunity to study the Kondo effect under conditions where the energy level spacing of the conduction electrons is larger than k_BT_K (vs. normally $\ll k_BT_K$ in extended systems) (68). Odom et al. tackled this question clearly by characterizing the DOS on and near Co clusters before and after cutting a SWNT host to $\sim$11 nm (21). The spectra recorded after

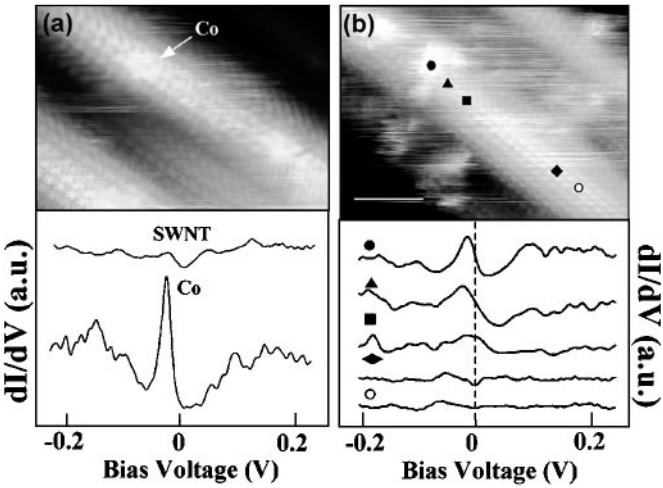

Figure 14 (*a*) Atomically resolved image of a 0.5 nm Co cluster on a SWNT, and dI/dV vs. V recorded at the position of the Co cluster and ∼7 nm away from cluster. (*b*) Constant current image of a larger Co cluster (∼1 nm) on a SWNT, and corresponding dI/dV vs. V measured at points indicated in the image. Adapted from Reference (21).

cutting showed the expected finite size eigenstates separated by ∼0.15 eV (3, 21), and also showed that the peak amplitude at E_F was markedly enhanced relative of the other level peaks. The enhanced conductance at E_F provides evidence of how sensitive the electronic properties of metallic nanotubes are to magnetic impurities, even in finite size structures where the level spacing is much larger than k_BT_K.

Lastly, these experiments suggest that metallic SWNTs are ideal hosts for studying basic features of the Kondo effect in 1D systems. However, the magnetic clusters (<1 nm) explored in this first report (21) also complicate analysis compared to the ideal of a single atom spin center. In this regard, future studies of the 1D Kondo effect could benefit substantially by using single magnetic atoms or molecules that have well-defined (and controllable) spin and can be registered precisely with respect to the underlying SWNT atomic lattice.

INTRAMOLECULAR JUNCTIONS

An exciting idea in the area of nanoscale electronic devices is to create intramolecular SWNT junctions. Theoretical work suggested early on that two different tubes could be connected seamlessly by interposing one or more pentagon-heptagon

(5/7) topologic defects between two nanotube segments of different helicity (69–74). Although some transport measurements (75) provided indirect evidence for the existence of proposed intramolecular junctions (IMJs), direct characterization of these potentially important structures was lacking until the recent work of Ouyang et al. (23).

Analysis of atomically resolved images has enabled the identification of IMJs (23). For example, the data in Figure 15*a* shows that the upper and lower portions of the nanotube have similar diameters (1.57 ± 0.07 nm) but significantly different chiral angles, where θ is $-3.9^\circ \pm 0.8^\circ$ and $-10.5^\circ \pm 0.8^\circ$ for the upper and lower portions, respectively. These data showed that the SWNT indices of the upper and lower regions were (21,−2) and (22,−5), respectively (23), and moreover, enabled the interface between SWNTs to be modeled (Figure 15*b*). Further strong evidence for this specific IMJ assignment was obtained from spectroscopy studies (Figure 15*c*), which showed that the upper and lower portions corresponded to a semiconductor and metal, respectively. Hence, these results show that this IMJ is a metal-semiconductor (M-S) junction—a potentially basic building block for nanoelectronics.

The detailed interface properties of this IMJ were also investigated by spatially resolved tunneling spectroscopy (Figure 15*c*). These measurements showed that this junction has a very sharp metal-semiconductor interface: the semiconducting VHS gap decays across the IMJ into the metallic segment within <1 nm, whereas the distinct spectroscopic features of the metallic tube appear to decay more quickly across the junction interface. Ouyang et al. used atomic models of the interface to compare calculated and experimentally measured DOS of this IMJ. Two low-energy structural models (Figure 15*b*), which contained three and four 5/7 pairs, were analyzed. Significantly, the local DOS (Figure 15*d*) obtained from tight-binding calculations for Model I agreed well with the measured local DOS across the IMJ interface, whereas Model II exhibited low-energy states around -0.10 eV not observed in experiment. Hence, it was possible to assign the structure of Model I as a reasonable representation for the observed (21,−2) − (22,−5) IMJ.

Ouyang et al. also characterized a metallic-metallic (M–M) IMJ using similar methods (23). These studies exhibited several new features compared to the M–S intramolecular junctions. First, atomic resolution images and subsequent analysis showed that the IMJ formed between SWNTs with substantial differences in diameter: 1.23 ± 0.05 nm and $d_t = 1.06 \pm 0.05$ nm, respectively. Second, this M–M IMJ exhibited localized states at -0.55 and -0.27 eV in the junction area, and both of these states decay on a nanometer length scale into the SWNTs on either side of the IMJ. These features contrast with the abrupt, clean M–S junction described above.

Direct atomically resolved characterization of IMJs by STM has important implications for applications because it provides a clear means for assessing synthetic efforts designed to prepare specific IMJs. We believe that such work could open

significant opportunity both for fundamental investigations of resonant scattering and for the controlled growth of intramolecular SWNT nanoelectronics devices.

CONCLUSIONS AND PROSPECTS

Scanning tunneling microscopy has proved an ideal tool to study the structural and electronic properties of individual and bundle SWNTs. Studies of defect-free SWNTs have shown that the electronic properties of nanotubes depend not only on radius and chirality but also on their detailed curvature and local environment. From a graphene based π-only tight-binding scheme, SWNTs with indices (n, n + 3q) should behave as metallic quantum wires. However, tunneling spectroscopy measurements made on metallic zigzag tubes showed energy gaps with magnitudes depending inversely on the square of the tube radius, whereas isolated armchair tubes do not have energy gaps and are truly metallic. In addition, armchair SWNTs in bundles exhibit pseudogaps at E_F due to tube-tube interactions that break the n-fold rotational symmetry of this system. STM was also used to determine directly the unique linear 1D energy dispersion of SWNTs through the analysis of resonant scattering and quantum interference. In addition, STM was exploited as a tool to create and investigate finite size effects in SWNTs. These studies show that it is possible to access readily a regime of "0D" behavior where finite length produces quantization along the tube axis. These results suggest future opportunities to probe, for example, connections between extended and molecular structures. As one of the applications of nanotubes as 1D systems, nanotubes were found to be ideal 1D hosts for the investigation of fundamental interactions between magnetic clusters and 1D electron systems. Lastly, direct atomically resolved characterization of intramolecular junctions in as grown SWNT samples by STM demonstrated the existence of IMJs and could have important implications for the controlled introduction of defects in nanoelectronic device applications.

We believe that this review has shown that many of the overall structural and electronic properties of SWNTs are now in hand, although this has really only opened the window to this fascinating 1D system. Future efforts promise to be rewarded with answers to very fundamental scientific questions, and importantly, these results should push from a firm intellectual footing the application of SWNTs in future nanotechnologies.

ACKNOWLEDGMENTS

We are indebted to our colleagues and collaborators. In particular, we thank Prof. H. Park, L.J. Lauhon, J.F. Wang, M.S. Gudiksen, and K. Kim for stimulating discussions, and thank T.W. Odom, P. Kim, and C.L. Cheung for their contributions to the work summarized herein. C.M.L. gratefully acknowledges support of this work by the Solid State Chemistry and Chemistry Divisions of the NSF.

LITERATURE CITED

1. Saito R, Dresselhaus G, Dresselhaus M. 1998. *Physical Properties of Carbon Nanotubes*. London: Imperial College
2. Dekker C. 1999. *Phys. Today* 52:22–28
3. Odom TW, Huang JL, Kim P, Lieber CM. 2000. *J. Phys. Chem. B* 104:2794–809
4. McEuen PL. 1998. *Nature* 393:15–16
5. Dai HJ, Hafner JH, Rinzler AG, Colbert DT, Smalley RE. 1996. *Nature* 384:147–50
6. Hafner JH, Cheung CL, Lieber CM. 1999. *Nature* 398:761–62
7. Treacy MMJ, Ebbesen TW, Gibson JM. 1996. *Nature* 381:671–74
8. Wong EW, Sheehan PE, Lieber CM. 1997. *Science* 277:1071–75
9. Mintmire JW, Dunlap BI, White CT. 1992. *Phys. Rev. Lett.* 68:631–34
10. Hamada N, Sawada S, Oshiyama A. 1992. *Phys. Rev. Lett.* 68:1579–82
11. Saito R, Fujita M, Dresselhaus G, Dresselhaus M. 1992. *Appl. Phys. Lett.* 60:2204–6
12. Saito R, Fujita M, Dresselhaus G, Dresselhaus M. 1992. *Phys. Rev. B* 46:1804–11
13. Odom TW, Huang JL, Kim P, Lieber CM. 1998. *Nature* 391:62–64
14. Wildöer JWG, Venema LC, Rinzler AG, Smalley RE, Dekker C. 1998. *Nature* 391: 59–62
15. Ouyang M, Huang JL, Cheung CL, Lieber CM. 2001. *Science* 292:702–5
16. Tans SJ, Devoret MH, Dai H, Thess A, Smalley RE, et al. 1997. *Nature* 386:474–77
17. Journet C, Maser WK, Bernier P, Loiseau A, Lamy de la Chapelle M, et al. 1997. *Nature* 388:756–59
18. Rao AM, Bandow S, Chase B, Eklund PC, Williams KW, et al. 1997. *Science* 275: 187–91
19. Kim P, Odom TW, Huang JL, Lieber CM. 1999. *Phys. Rev. Lett.* 82:1225–28
20. Venema LC, Wildöer JWG, Janssen JW, Tans SJ, Tuinstra HLJT, et al. 1999. *Science* 283:52–55
21. Odom TW, Huang JL, Cheung CL, Lieber CM. 2000. *Science* 290:1549–52
22. Ouyang M, Huang JL, Lieber CM. 2001. *Phys. Rev. Lett.* 88:066804-1-4
23. Ouyang M, Huang JL, Cheung CL, Lieber CM. 2001. *Science* 291:97–100
24. Wallace PR. 1947. *Phys. Rev.* 71:622–34
25. Ashcroft NW, Mermin ND. 1976. *Solid State Physics*. New York: Holt, Rinehart & Winston
26. Rubio A. 1999. *Appl. Phys. A* 68: 275–82
27. Mintmire JW, Robertson DH, White CT. 1993. *J. Phys. Chem. Solids* 54:1835–40
28. Mintmire JW, White CT. 1998. *Phys. Rev. Lett.* 81:2506–9
29. Blasé X, Benedict LX, Shirley EL, Louie SG. 1994. *Phys. Rev. Lett.* 72:1878–81
30. White CT, Robertson DH, Mintmire JW. 1996. In *Clusters and Nanostructures Materials*, ed. P Jena, S Behera, pp. 231–37. New York: Nova
31. Kane CL, Mele EJ. 1997. *Phys. Rev. Lett.* 78:1932–35
32. Kleiner A, Eggert S. 2001. *Phys. Rev. B* 63: 734081–84
33. Yang L, Han J. 2000. *Phys. Rev. Lett.* 85: 154–57
34. White CT, Mintmire JW. 1998. *Nature* 394:29–30
35. Delaney P, Choi HJ, Ihm J, Louie SG, Cohen ML. 1998. *Nature* 391:466–69
36. Delaney P, Choi HJ, Ihm J, Louie SG, Cohen ML. 1999. *Phys. Rev. B* 60:7899–904
37. Maarouf AA, Kane CL, Mele EJ. 2000. *Phys. Rev. B* 61:11156–65
38. Kwon YK, Saito S, Tomanek D. 1998. *Phys. Rev. B* 58:13314–17
39. Odom TW, Huang JL, Kim P, Ouyang M, Lieber CM. 1998. *J. Mater. Res.* 13:2380–87
40. Crommie MF, Lutz CP, Eigler DM. 1993. *Nature* 363:524–27

41. Hasegawa Y, Avouris Ph. 1993. *Phys. Rev. Lett.* 71:1071–74
42. Kanisawa K, Butcher MJ, Yamaguchi H, Hirayama Y. 2001. *Phys. Rev. Lett.* 81: 3384–87
43. Yokoyama T, Okamoto M, Takayanagi K. 1998. *Phys. Rev. Lett.* 81:3423–26
44. Clauss W, Begeron DJ, Freitag M, Kane CL, Mele EJ, Johnson AT. 1999. *Europhys. Lett.* 47:601–7
45. Hassanien A, Tokumoto M, Umek P, Mihailovic D, Mrzel A. 2001. *Appl. Phys. Lett.* 78:808–10
46. Choi HJ, Ihm J, Louie SG, Cohen ML. 2000. *Phys. Rev. Lett.* 84:2917–20
47. Bockrath M, Liang W, Bozovic D, Hafner JH, Lieber CM, et al. 2001. *Science* 291: 283–85
48. Burgi L, Jeandupeux O, Brune H, Kern K. 1999. *Phys. Rev. Lett.* 82:4516–19
49. Lemay SG, Janssen JW, van den Hout M, Mooij M, Bronikowski MJ, et al. 2001. *Nature* 412:617–20
50. Mizes HA, Foster JS. 1989. *Science* 244: 559–62
51. Lannoo M, Friedel P. 1991. *Atomic and Electronic Structure of Surfaces*. Berlin: Springer-Verlag
52. Dresselhaus MS, Dresselhaus G, Eklund PC. 1996. *Science of Fullerene and Carbon Nanotubes*. San Diego: Academic
53. de Heer WA, Chatelain A, Ugarte D. 1995. *Science* 270:1179–82
54. Collins PG, Zettle A. 1996. *Appl. Phys. Lett.* 69:1969–72
55. de Heer WA, Bonad J, Fauth K, Chatelain A, Forro L, Ugarte D. 1997. *Adv. Mater.* 9: 87–92
56. Venema LC, Wildöer JWG, Tuinstra HLJT, Dekker C, Rinzler A, Smalley RE. 1997. *Appl. Phys. Lett.* 71:2629–32
57. Rubio A, Sanchez-Portal D, Attach E, Ordoejon P, Soler JM. 1999. *Phys. Rev. Lett.* 82:3520–23
58. Bulusheva LG, Okotrub AV, Romanov DA, Tomanek D. 1998. *J. Phys. Chem. A* 102:975–81
59. Rochefort A, Salahub DR, Avouris PH. 1999. *J. Phys. Chem. B* 103:641–46
60. Odom TW, Hafner JH, Lieber CM. 2001. *Top. Appl. Phys.* 80:173–211
61. Deleted in proof
62. McEuen PL, Bockrath M, Cobden DH, Yoon YG, Louie SG. 1999. *Phys. Rev. Lett.* 83:5098–101
63. Jishi RA, Bragin J, Lou L. 1999. *Phys. Rev. B* 59:9862–65
64. Kondo J. 1964. *Prog. Theor. Phys.* 32:37–87
65. Li J, Schneider WD, Berndt R, Delley B. 1998. *Phys. Rev. Lett.* 80:2893–96
66. Madhavan V, Chen W, Jamneala T, Crommie MF, Wingreen NS. 1998. *Science* 280:567–70
67. Manoharan HC, Lutz CP, Eigler DM. 2000. *Nature* 403:512–15
68. Wolfgang B, Thimm JK, von Delft J. 1999. *Phys. Rev. Lett.* 82:2143–46
69. Dunlap BI. 1994. *Phys. Rev. B* 49:5643–51
70. Charlier JC, Ebbesen TW, Lambin PH. 1996. *Phys. Rev. B* 53:11108–13
71. Chico L, Benedict LX, Louie SG, Cohen ML. 1996. *Phys. Rev. B* 54:2600–6
72. Saito R, Dresselhaus G, Dresselhaus MS. 1996. *Phys. Rev. B* 53:2044–50
73. Lambin PH, Fonseca A, Vigneron JP, Nagy JB, Lucas AA. 1995. *Chem. Phys. Lett.* 76:971–74
74. Chico L, Benedict LX, Louie SG, Cohen ML. 1996. *Phys. Rev. Lett.* 76:971–74
75. Yao Z, Postma HWCh, Balents L, Dekker C. 1999. *Nature* 402:273–76

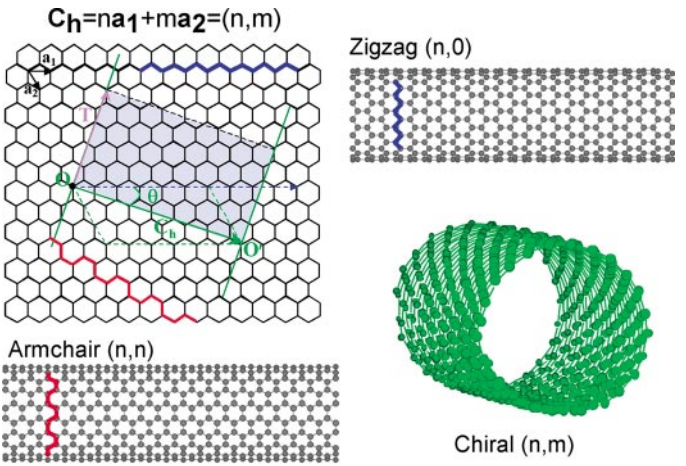

Figure 1 Schematics of graphene sheet and typical SWNTs structures. OO′ defines the chiral vector $\mathbf{C}_h = n\mathbf{a}_1 + m\mathbf{a}_2 \equiv (n,m)$. Translation vector, **T**, is along the nanotube axis and perpendicular to the $\mathbf{C}_h$. The shaded, area represents the unrolled unit cell formed by **T** and $\mathbf{C}_h$. Chiral angle, θ, is defined as the angle between the $\mathbf{C}_h$ and (n,0) zigzag direction. Two limiting achiral cases of (n,0) zigzag and (n,n) armchair SWNTs are indicated in *blue* and *red*, respectively. Molecular models of typical armchair, zigzag and chiral SWNTs are also shown.

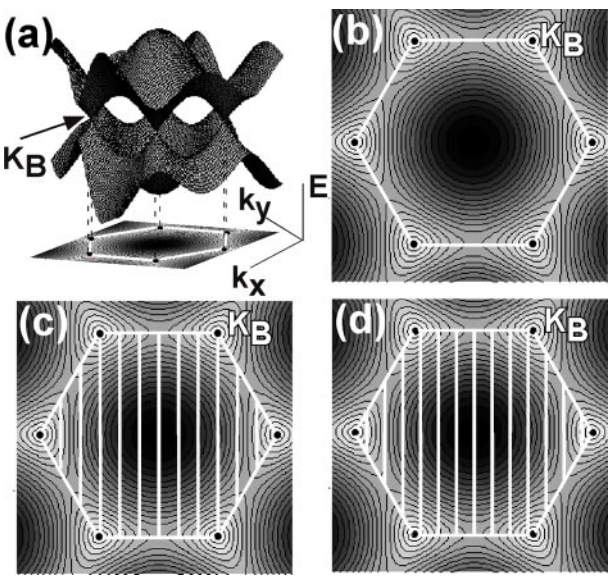

Figure 2 (*a*) Three-dimensional plot of the π and π^* graphene energy bands and (*b*) a 2D projection. (*c*) Allowed 1D wavevectors for a metallic (9,0) SWNT. (*d*) Allowed 1D wavevectors for a semiconducting (10,0) tube. The *white hexagons* define the first Brillouin zone of a graphene sheet, and the *black dots* in the corners are the $\mathbf{K}_B$ points.

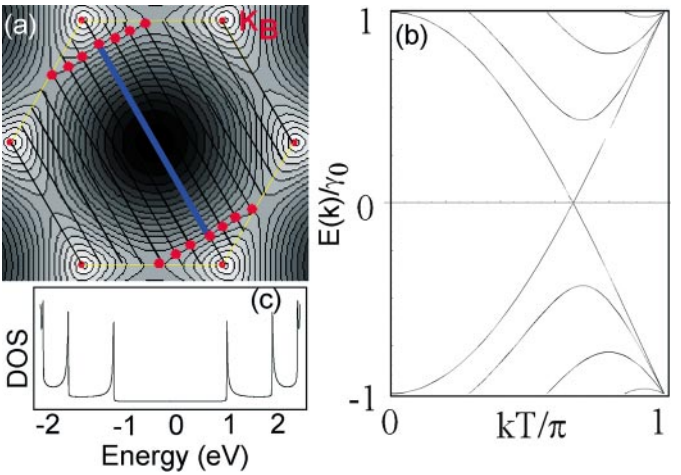

Figure 3 (*a*) Zone-folded representation of the 1D subbands for a (7,7) SWNT. The distance between the *red dots* segmenting these *parallel black lines* represents the size of the Brillouin zone, with the first Brillouin zone indicated by the *blue bold line*. The *small red dots* at the corners of graphene's hexagonal Brillouin zone are the graphene $\mathbf{K}_B$ points. (*b*) Energy dispersion for the (7,7) SWNT described in the zone-folding representation. (*c*) DOS calculated from a graphene based π-only tight-binding scheme.

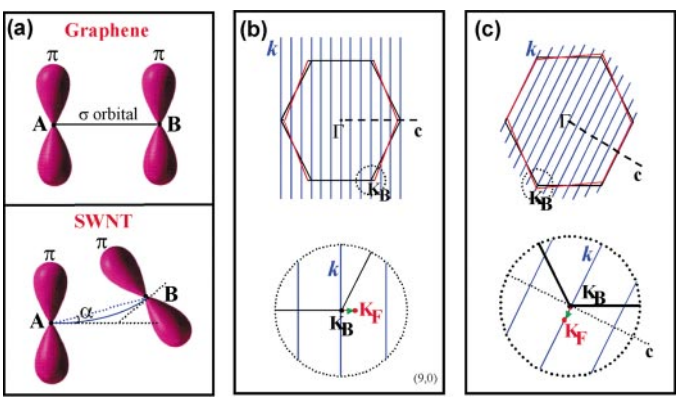

Figure 4 (*a*) (*top*) A and B denote two nearest neighbor parallel π orbitals on a flat graphene sheet. (*bottom*) Corresponding π orbitals on a curved surface, where α is the angle between the π orbitals. (*b*) (*top*) Hexagonal Brillouin zone of graphene sheet is defined by *black lines*. *Blue lines* are the allowed wavevectors $\boldsymbol{k}$ of (9,0) zigzag SWNTs, which are parallel to the tube axis. *Red lines* represent the effect of curvature. **c** is the circumferential direction perpendicular to the tube axis. (*bottom*) Fermi point shift is indicated in *red* for a "metallic" zigzag SWNTs; $\boldsymbol{k}_F$ moves along the **c** direction away from the graphene's $\mathbf{K}_B$ point. (*c*) Same as (*b*) but for case of armchair SWNT. For armchair SWNTs, $\boldsymbol{k}_F$ moves along the tube axis direction away from the $\mathbf{K}_B$ point.

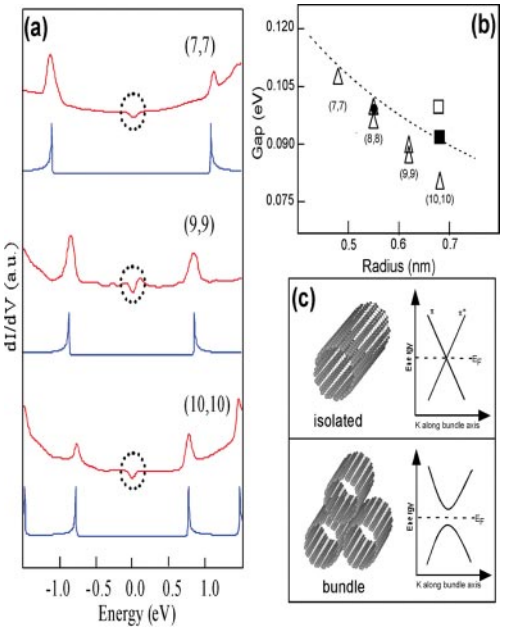

Figure 8 (*a*) Tunneling conductance data, dI/dV, for different armchair SWNTs in bundles, with corresponding calculated DOS shown below each experimental curve. The new features in the low energy region of the (7,7), (9,9), and (10,10) tubes are highlighted by *dashed circles*. (*b*) Summary of the observed pseudogaps vs. tube radius. Each experimental data point (*triangle*) represents an average gap value measured on a distinct (n,n) tube. Theoretical results are also shown for comparison: the *solid square* and *dashed line* correspond, respectively, to the gap value of a (10,10) tube and radius dependence of the gap widths (37); the *open square* is for a (10,10) tube from (35, 36). And the *solid circle* shows the value calculated for an (8,8) tube (26). The (10,10) result from (38), ∼200 meV, is off the scale. (*c*) Models of an isolated (8,8) SWNT and bundle of three (8,8) tubes, and corresponding schematics of the π and π^* bands near E_F.

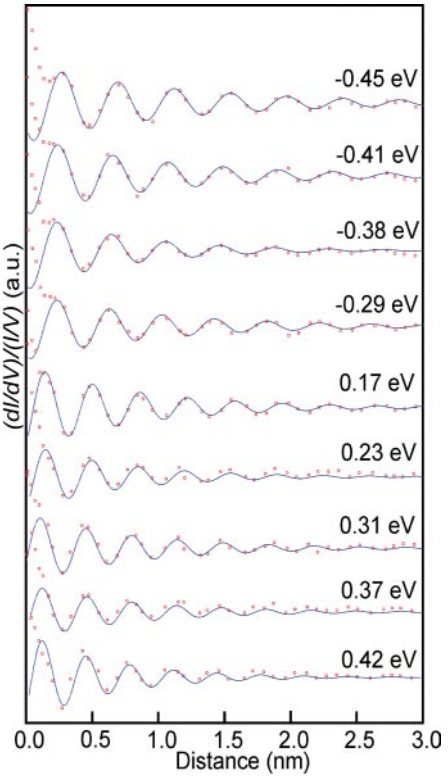

Figure 11 Spatial oscillation of $(dI/dV)/(I/V)$ at all observed nine energies. The origin represents the defect position, which corresponds to the white arrow in Figure 9. *Red open circles*: experimental data; *blue solid lines*: theoretical fits of Eq. 11 to the data. The fitting parameters [k (nm^{-1}), δ, l_φ (nm)] for data recorded at -0.45, -0.41, -0.38, -0.29, 0.17, 0.23, 0.31, 0.37 and 0.42 eV are [7.45, -3.82, 1.82], [7.59, -3.48, 1.82], [7.72, -3.49, 2.84], [7.97, -3.48, 2.08], [8.69, -2.32, 1.82], [8.85, -2.22, 1.80], [8.99, -1.95, 1.55], [9.16, -1.84, 1.74], [9.32, -1.99, 1.37], respectively.

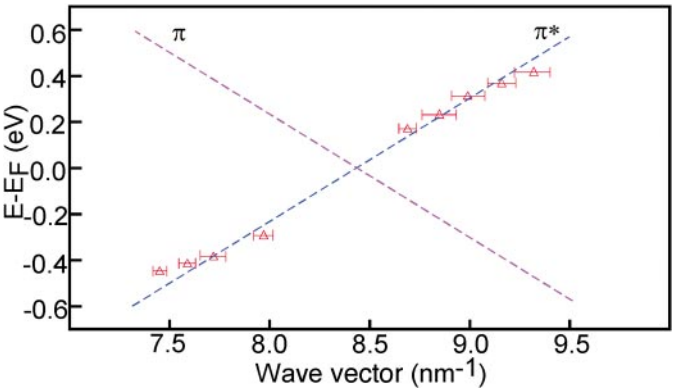

Figure 12 Energy dispersion near E_F for the (13,13) armchair SWNT. The experimental data points are *red triangles*, and the calculated bands are *dashed lines*.

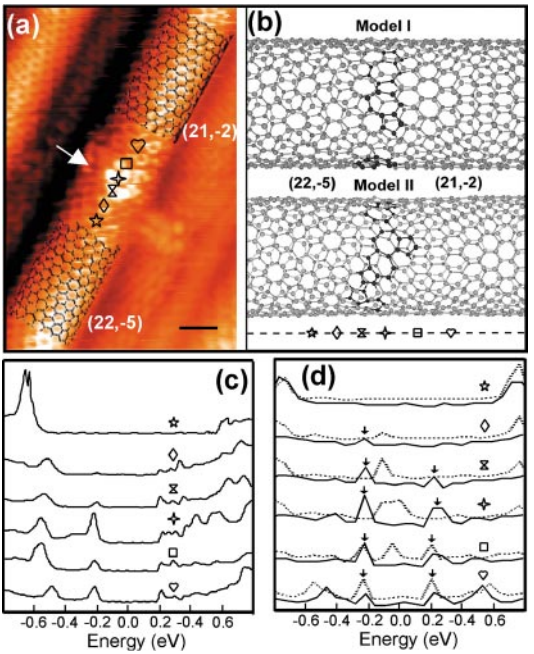

Figure 15 (*a*) Atomically resolved STM image of a SWNT containing an IMJ, which is highlighted with a *white arrow*. *Black honeycomb meshes* corresponding to (21, −2) and (22, −5) indices are overlaid on the *upper* and *lower* portions, respectively, to highlight the distinct atomic structures of the different regions of the SWNT. Scale bar, 1 nm. (*b*) Model I has three separated 5/7 pairs, and Model II has two isolated 5/7 pairs, and one 5/7-7/5 pair. The *solid black spheres* highlight the atoms forming the 5/7 defects. (*c*) Spatially resolved dI/dV data acquired across the M-S IMJ at the positions indicated by six symbols in (*a*). (*d*) Calculated local DOS for Model I (*solid line*) and for Model II (*dashed line*). The *arrows* highlight the same features as in (*c*).